



In Collaboration with  
the Netherlands Institute for Sea Research

**JOURNAL OF  
SEA RESEARCH**

Journal of Sea Research 47 (2002) 209–222

www.elsevier.com/locate/seares

# Internal wave band kinetic energy production: flat vs. sloping bottom

Johannes R. Gemmrich\*, Hans van Haren

*Netherlands Institute for Sea Research (NIOZ), PO Box 59, 1790 AB Den Burg, Texel, The Netherlands*

Received 23 March 2001; accepted 17 September 2001

## Abstract

Velocity and temperature measurements obtained with acoustic Doppler current profilers and thermistor strings are used to evaluate the production of internal wave band kinetic energy mainly in the frequency band  $\sigma > 15$  cpd. Results from a flat 19 m deep, vigorous tidal environment in a shelf sea are compared with energy production in a bottom boundary layer above a continental slope. In the tidal environment, maximum production occurs in the near-bottom and near-surface layers. A distinct mid-depth maximum in KE production occurs during a period when wind speeds exceed  $10 \text{ m s}^{-1}$  and significant wave height  $\sim 2$  m. At the same time, no significant changes in the along-shore current speed take place but the cross-shore current, generated by strong stratification, is weakened. This suggests a direct energy input from the wind via surface waves into the water column turbulence. Maximum kinetic energy production in the frequency band  $\sigma > 1.9$  cpd, thus including the semidiurnal tide, occurs at mid-depth when strong stratification is present. The overall magnitude of internal wave band kinetic energy production agrees well with independent dissipation estimates obtained from microstructure profilers. Above the sloping bottom, KE production is somewhat *larger* than observed in the shallow tidal environment, despite rms currents being  $\sim 50\%$  *smaller* and wind effects being small. Above the sloping bottom KE shear production was comparable to buoyancy production. The latter was negligible at the shelf sea site. Crown Copyright © 2002 Published by Elsevier Science B.V. All rights reserved.

*Keywords:* Southern North sea; Bay of Biscay; Internal wave band; Kinetic energy production

## 1. Introduction

Shallow shelf seas with vigorous tidal currents represent one of the most energetic oceanic environments. A primary example is the southern North Sea where water depths are less than 20 m up to 20 km offshore and tidal currents reach up to  $1.5 \text{ m s}^{-1}$ .

These strong currents may generate vigorous vertical exchange of water masses, which affects air-sea exchange of heat and gas, biological productivity as well as sedimentation rates. Mixing is primarily associated with bottom friction and may be enhanced (or dampened) due to stratification introduced by river outflows. During frequent periods of high wind speeds, wind and wave induced mixing may also affect the entire water column. As part of the European Union research project PROCesses of Vertical Exchange in Shelf Seas (PROVESS) mixing processes in this environment have been investigated.

\* Corresponding author. Present affiliation: Institute of Ocean Sciences, PO Box 6000, Sidney, BC, V8L 4B2, Canada.

*E-mail address:* Gemmrichj@pac.dfo-mpo.gc.ca (J.R. Gemmrich).

Contrasting environments are regions above sloping bottom boundaries, although they are thought to have high mixing rates too. There is evidence that, due to internal wave reflection, turbulent mixing rates above sloping bottoms are much higher than above flat bottoms with similar current structures (Eriksen, 1985; Ivey and Nokes, 1989; DeSilva et al., 1998; Gemmrich and Van Haren, 2002). Internal waves reflecting from a sloping boundary preserve their frequency and incident and reflected wave propagate at the same angle to the vertical rather than the same angle to the boundary. Near critical conditions, where the bottom slope matches the inclination of the group velocity vector of the reflected wave, current shear increases and wave breaking and consequently enhanced mixing may occur.

Central to the issue of boundary layer mixing are profiles of momentum fluxes and buoyancy fluxes. Combining flux profiles with velocity shear profiles, the rate of kinetic energy production  $P$  available for mixing can be inferred:

$$P = \overline{u' w'} \frac{\partial \bar{u}}{\partial z} + \overline{v' w'} \frac{\partial \bar{v}}{\partial z} + \overline{w' w'} \frac{\partial \bar{w}}{\partial z} + \overline{g b' w'} \quad (1)$$

where  $u$ ,  $v$ ,  $w$  are orthogonal current components,  $b$  is the local buoyancy and  $g$  is the gravitational acceleration. The overbar represents a time average and the prime denotes fluctuating quantities, separating each record into two parts using Reynolds-decomposition. The first three terms on the right-hand side of (1) represent the kinetic energy production due to Reynolds stresses (shear production) and the last term the conversion of potential energy into kinetic energy (buoyant production), which may be negative.

Here we present results from 7-d observations of temperature and current fields in the southern North Sea in April 1999 (PROVESS99). These results are compared with a 7-d subset of similar observations acquired in the near-bottom layer above the continental slope in the Bay of Biscay in July 1996 (BBB96). Details of this data set with emphasis on evaluation of boundary layer dynamics and the effect of internal wave-band fluxes are given in Gemmrich and Van Haren (2002).

Data were obtained from a specially designed thermistor string (Van Haren et al., 2001) and acoustic Doppler current profilers (ADCP). The instrumentation

measured variations of all three velocity components and temperature fluctuation at typically 0.5 or 1 m vertical resolution and 20 s or 30 s sampling intervals (depending on deployment). As a result, momentum and buoyancy fluxes supported by larger scale eddies in the internal wave band are estimated, but not turbulence at dissipation scales.

## 2. Observations

Depending on the specific requirement for any given experiment a bottom lander is equipped with one or two rigidly mounted ADCP's, a thermistor string and a tiltmeter.

### 2.1. Shelf sea observations

During PROVESS99 the instrumentation was deployed in the southern North Sea at 52°18.1' N, 4°18.0' E at a water depth of 19 m. An upward looking 600 kHz ADCP rendered velocities between 2.65 m–14.65 m above the bottom at 0.5 m vertical bin resolution. Note that no useful velocities could be obtained at 10.65–12.65 m, due to interference with the buoyancy float of the thermistor string. The thermistor string with 32 sensors at 1 m spacing each (Van Haren et al., 2001) was back-folded three times resulting in somewhat uneven spacing ranging from 0.18 m to 0.3 m. It included a tiltmeter at its upper end. The lowest thermistor was located at 0.97 m. Due to swaying of the thermistor string in the strong tidal currents, the maximum vertical extent of the thermistor string varied by up to 2 m. In the following, the temperature records have been interpolated onto a regular depth grid, matching the ADCP velocity bins. The necessary sensor depth corrections are based on the recorded tilt of the thermistor string. Temperature and velocity field were sampled at a rate of once per 20 s. The deployment period was 1 to 8 April 1999 (yeardays 91–98).

The deployment site, ~15 km offshore, has a relatively flat bottom topography. The coastline is very regular and strongest currents are parallel to the coast. Therefore, a natural, right-handed co-ordinate system is adopted with the x-axis being perpendicular (on-shore) and positive towards shore and the y-axis parallel (along-shore) to an idealised straight coast-

line. The vertical axis is positive upwards from the bottom ( $z=0$ ). Data were transformed accordingly.

The PROVESS99 site is dominated by strong semidiurnal tidal currents and a semidiurnal tidal stratification cycle, introduced by freshwater outflow

further to the south (Simpson and Souza, 1995). The along-shore current component reached  $\pm 1.2 \text{ m s}^{-1}$  uniformly throughout the monitored water column and with little variation during the deployment period (Fig. 1). Maximum on-shore currents are  $\pm 0.3 \text{ m s}^{-1}$ .

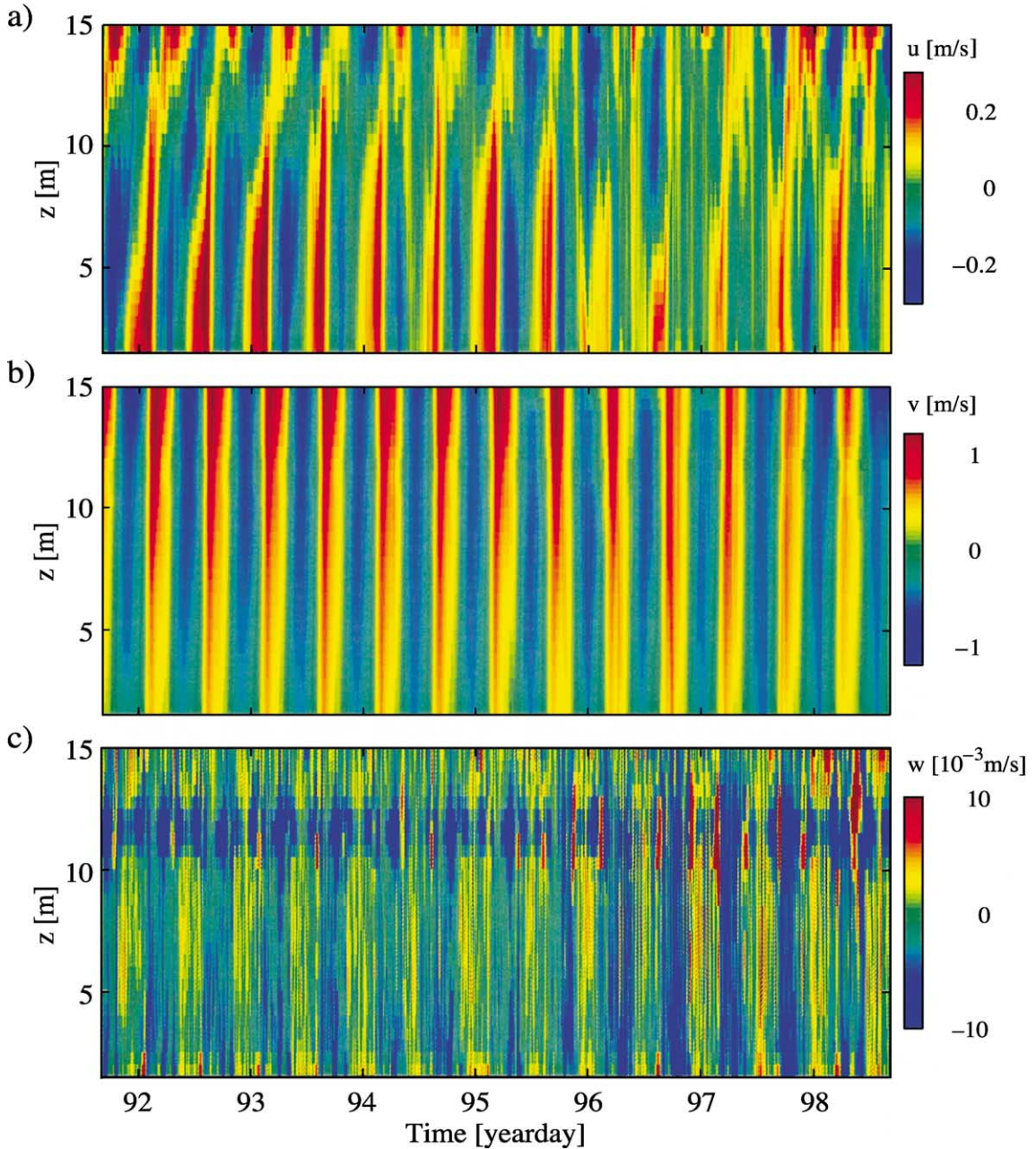


Fig. 1. Current field at PROVESS99. (a) on-shore velocity  $u$ , (b) along-shore velocity  $v$  and (c) vertical velocity  $w$ .

The structure of the on-shore current field changed at yearday 96. At the beginning of the experiment the stratification cycle, associated with tidal straining, generated a strong on-shore velocity shear, with opposing currents in the upper half and the lower half of the water column, characteristic for this area (Visser et al., 1994). From day 96 on, this current pattern weakened, due to wind and wave-induced mixing (Fig. 2). Noticeably smaller on-shore currents combined with somewhat reduced off-shore flows resulted in a weaker velocity shear, in response to weaker stratification.

Vertical velocities described a semidiurnal tidal alternation between sinking and rising, i.e. settling and suspension of particles. Maximum vertical velocities reached  $\sim 10^{-2} \text{ m s}^{-1}$ . Sinking velocities were

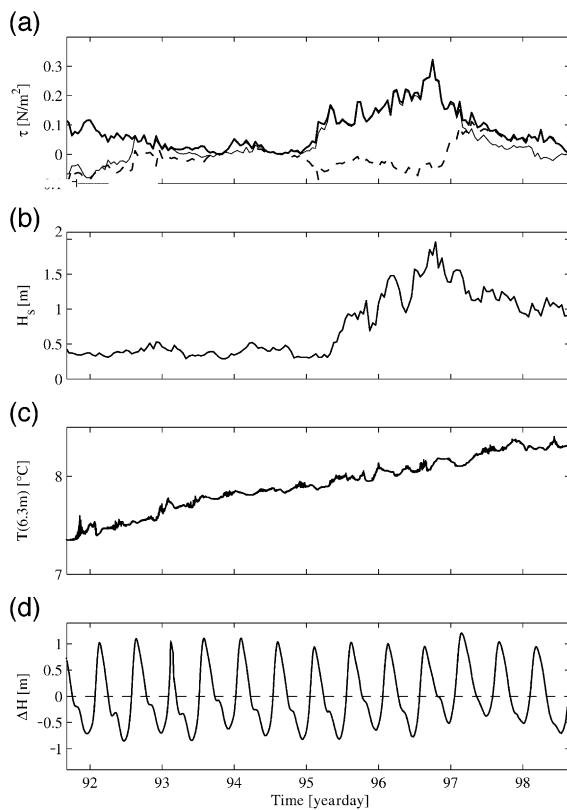


Fig. 2. Environmental conditions during PROVESS99. (a) wind stress  $\tau$ , total (thick line), along-shore component (thin line), on-shore component (dashed line), (b) significant wave height  $H_s$ , (c) water temperature  $T$  at 6.3 m above the bottom and (d) tidal elevation  $\Delta H$ .

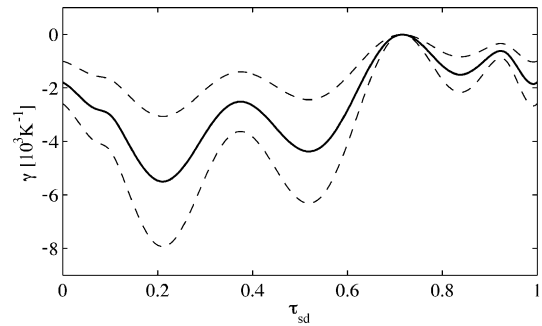


Fig. 3. Depth-time average of effective thermal expansion factor  $\gamma$  (solid line) as function of semidiurnal tidal period  $\tau_{sd}$ . Dashed lines show uncertainties based on temporal variations (see text).

generally somewhat larger than upward currents. Erroneous vertical velocity readings may result from incomplete tilt correction of the instrument head. According to the manufacturer's manual tilt accuracy  $\Delta\theta < 1^\circ$ , so that we may expect  $\Delta w \propto u \sin\theta < 0.02u$ . To check whether the observed vertical velocities were biased by horizontal currents we calculated the correlation between vertical and horizontal currents in along-shore and cross-shore direction for each velocity bin. A correlation consistent throughout all depths may indicate a bias. However, in along-shore direction the correlation decreased rapidly with height and in cross-shore direction the correlation changed sign at  $\sim 5$  m. Therefore, we expect the recorded vertical velocities to represent true vertical velocities (averaged over the beam spread). The 7-d mean value is  $-2 \times 10^{-3} \text{ m s}^{-1}$ , which compares favourably with observed particle settling rates (McCandliss et al., 2002). The consistency of the vertical velocity over tens of minutes implies a complete turnover between bottom and surface water within each tidal cycle for this shallow water depth.

The one-week deployment period covered a range of meteorological conditions (Fig. 2). The beginning is characterised by low wind speed, stable stratification and low air-sea exchange of heat, moisture and momentum. At yearday 95 a low pressure system moved through the area and the wind speed increased to  $12 \text{ m s}^{-1}$ . The significant wave height  $H_s$ , recorded at the nearby research platform Noordwijk, increased from  $H_s < 0.5$  m prior to yearday 95 to  $H_s \sim 2$  m on yearday 96. Mainly due to sensible heat exchange, the

water temperature increased steadily by  $\sim 1$  K over the one-week deployment period. The tidal elevation at the site was  $\sim 2$  m.

*2.1.1. Stratification effects*

On yearday 94–96, CTD-profiles were acquired in the vicinity of the deployment site at approximately 1-h intervals. They reveal a strong semidiurnal tidal

cycle in salinity and temperature. Strongest vertical gradients, occurring at slack tide, reach  $0.02 \text{ K m}^{-1}$  and  $0.06 \text{ psu m}^{-1}$  for temperature and salinity, respectively.

We are interested in vertical buoyancy fluxes  $\overline{b' w'}$  to estimate the energy available for mixing processes. Therefore, variations in the recorded temperature field were related to the associated density field. For a

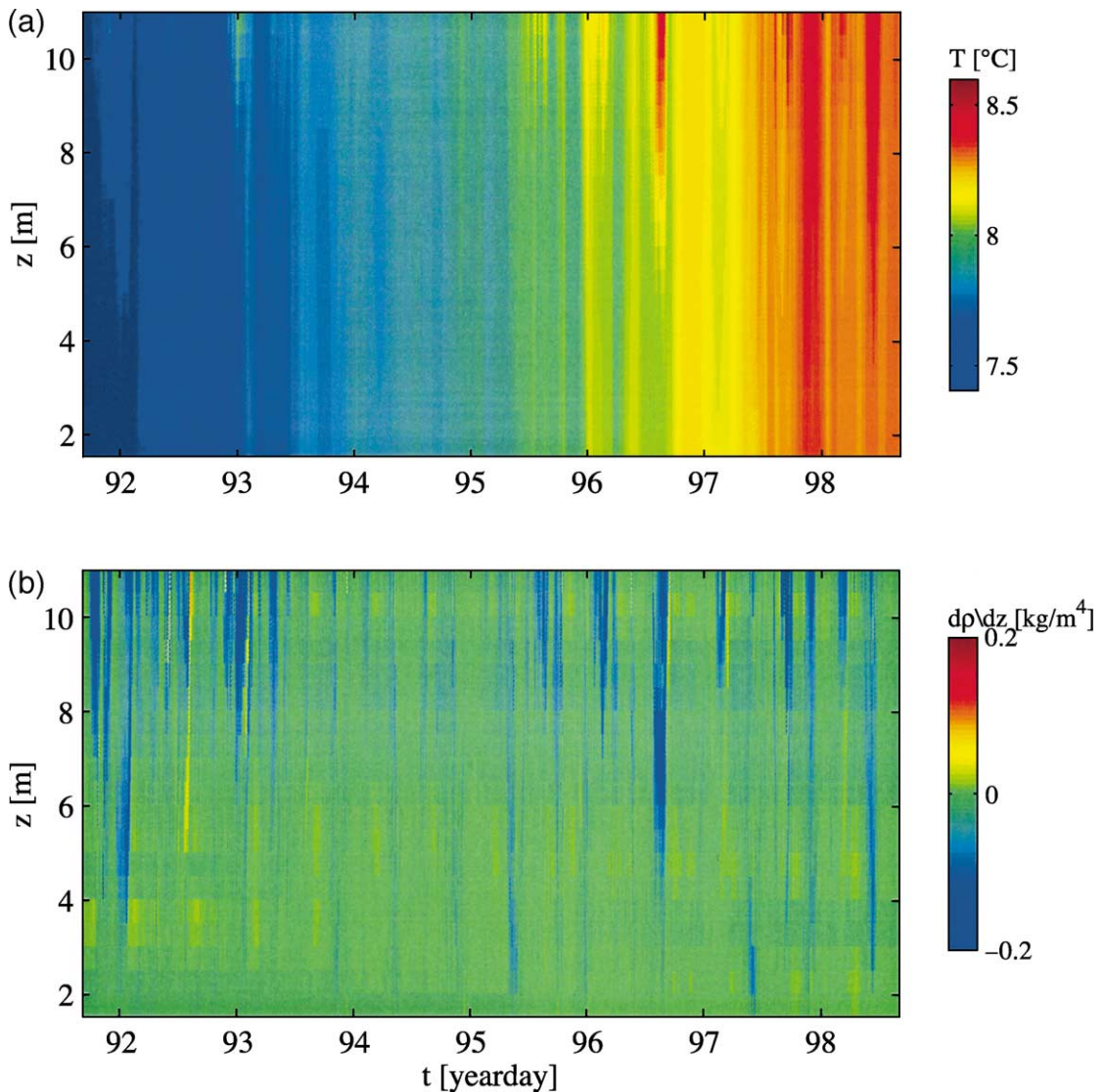


Fig. 4. (a) Temperature field at PROVESS99. (b) Density gradients at PROVESS99. Density variations are inferred from measured temperatures variations multiplied by the average temperature-density relationship presented in Fig. 3.

known tight T-S relationship, density fluctuations may be inferred from either temperature or salinity records. However, at the PROVESS99 site the temperature-density (T- $\sigma$ ) relation is a strong function of tidal phase, as inferred from all 32 available CTD-profiles

and mapped onto the semidiurnal tidal phase corresponding to the time the CTD profile was recorded. The depth-time average of the obtained T- $\sigma$  relations represents an effective thermal expansion coefficient  $\gamma$  which combines thermal as well as salinity effects

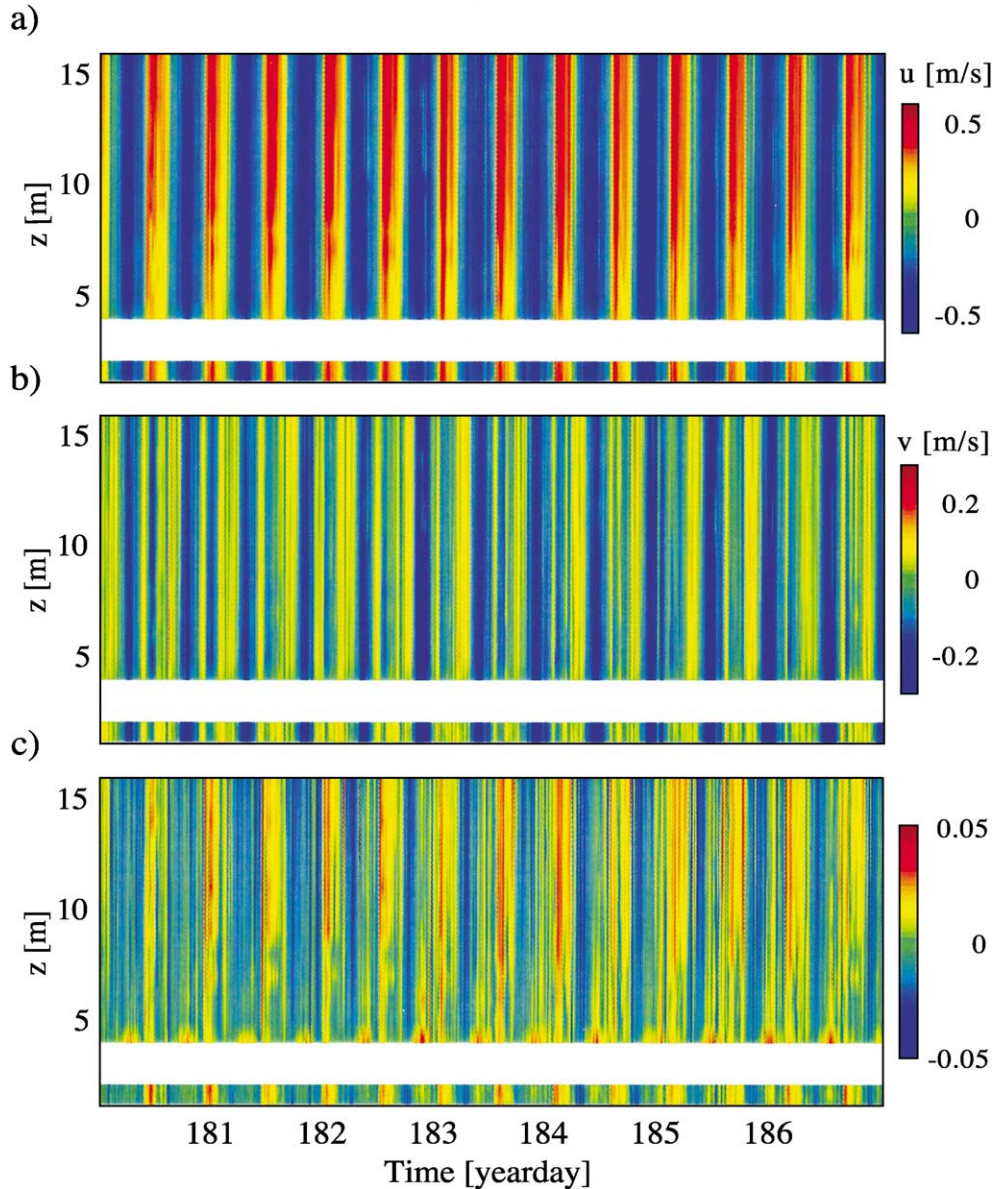


Fig. 5. Current field at BBB96. (a) along-slope velocity  $u$ , (b) cross-slope velocity  $v$  and (c) bottom-normal velocity  $w$ . The white band indicates no data between ranges of up- and down-ward looking ADCP's.

(Fig. 3). The density is given as  $\rho = \rho_0(1 + \gamma T)$ , where  $\rho_0$  is a reference density. Due to salinity contributions, the average value  $\gamma = 2.5 \times 10^{-3} \text{ K}^{-1}$  is more than one order of magnitude larger than the thermal expansion coefficient  $\alpha = 1.4 \times 10^{-4} \text{ K}^{-1}$ . The effective thermal expansion coefficient  $\gamma$  shows a semidiurnal shape with a superimposed first harmonic and values ranging from approximately  $-5.5 \times 10^{-3} \text{ K}^{-1}$  to  $-1 \times 10^{-4} \text{ K}^{-1}$ . This effective thermal expansion coefficient is based on the assumption of a depth-independent T- $\sigma$  relationship and can therefore provide only a first order estimate of the true T- $\sigma$  relation. The average error originating from temporal variations between tidal cycles is  $\sim 44\%$ .

Transforming the observed temperature record (Fig. 4a) using  $\gamma(t)$  yields an estimate of the local stratification (Fig. 4b). Generally, the near-bottom layer is well-mixed and at the beginning of the deployment period strong stratification is found at the thermocline at  $\sim 10$  m. On days 93.5–95.5, no significant stratification was found in the observed water column up to 11 m. During the period of higher wind speed, enhanced stratification is confined within short time periods of  $\sim 1$ -h duration around the time of along-shore flow reversal.

## 2.2. Observations on the continental slope

Continuous measurements of temperature and velocity structure were obtained for a period of 22 days in 1996 in a layer of 50 m above the bottom of the continental slope in the Bay of Biscay at  $48^\circ 37.8' \text{ N}$ ,  $8^\circ 19.9' \text{ W}$  at 800 m depth (BBB96) (Gemmrich and Van Haren, 2002). Here, only a subset of the BBB96 data, covering a 7-d period centred around spring tide, is studied. Furthermore, we restrict the vertical extent to 15 m above the bottom. During BBB96 a bottomlander was equipped with an upward-looking 600 kHz ADCP with 1 m vertical bin resolution and a downward-looking 1200 kHz ADCP with 0.25 m vertical bin resolution. The thermistor string provided temperature profiles between 2.9 m and 33.9 m at 1-m vertical resolution. Sampling rate for all sensors was once per 30 s.

The mean slope at the deployment site is  $\alpha = 4.7^\circ$  and is larger than the estimated local critical slope for semidiurnal internal tides  $\alpha_{\text{cr}} = 2.9^\circ \pm 1^\circ$ . The BBB96 data were transformed into a bottom-oriented co-

ordinate system. The x-direction is aligned with the isobaths (along-slope), the y-direction is cross isobaths and positive towards shallower water (cross-slope) and the vertical axis is bottom-normal and positive away from the bottom.

At all depths within the measurement range temperature and velocity fields are dominated by semidiurnal tidal fluctuations  $M_2$ . The cross-slope velocity component  $v$  exhibits an equally large  $M_4$  component. Maximum values of along-slope, cross-slope and vertical current components are  $u = \pm 0.6 \text{ m/s}$ ,  $v = \pm 0.25 \text{ m/s}$ ,  $w = \pm 0.06 \text{ m s}^{-1}$ , respectively (Fig. 5). Thus, maximum currents for BBB96 are approximately half the size of those observed during PROVESS99. All three current components are in phase throughout the monitored water column. Associated with the current fluctuations are semidiurnal temperature fluctuations of up to 2 K within one tidal period (Fig. 6). Thermal stratification varies with  $M_2$  periodicity between weak stratification  $O(10^{-4} \text{ K m}^{-1})$  and vertical temperature gradients up to  $4 \times 10^{-2} \text{ K m}^{-1}$ . The latter value is twice as large as during PROVESS99. However, using a constant T-S relationship found at the beginning of the deployment period, density variations are generally smaller for BBB96 due to the weaker contribution of salinity gradients. The observed upward phase propagation of the temperature field and currents is consistent with internal waves generated at the shelf break having downward energy propagation (Gemmrich and Van Haren, 2002).

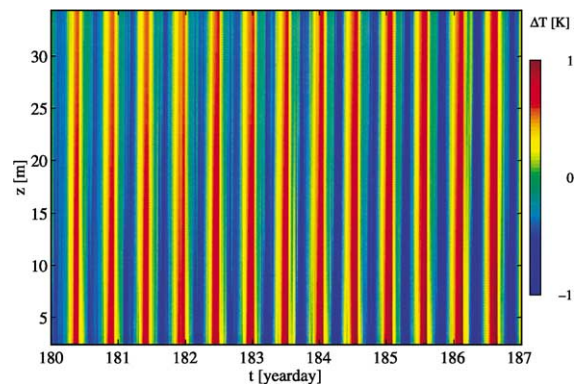


Fig. 6. Temperature fluctuations (high-pass filtered at 1.9 cpd) at BBB96. Density fluctuation may be inferred as  $\rho_0 \alpha \Delta T$ , with  $\alpha = 1.7 \times 10^{-4} \text{ K}^{-1}$  and reference density  $\rho_0$ .

### 3. Momentum fluxes and kinetic energy production

#### 3.1. Momentum fluxes

The focus of this study is the comparison of the kinetic energy production (1) for the two contrasting environments. Therefore, first the vertical eddy fluxes of momentum and buoyancy have to be determined. The method of inferring eddy momentum fluxes from ADCP measurements was pioneered by Lohrmann et al. (1990). It was applied to estimate fluxes above sloping bottom topography (Van Haren et al., 1994; Gemmrich and Van Haren, 2002) and in a tidal channel (Lu and Lueck, 1999). A combination of ADCP measurements with thermistor string observations may additionally yield heat fluxes (Van Haren et al., 1994; Gemmrich and Van Haren, 2002). Here we give a summary of the method.

Vertical eddy fluxes of  $x$ - and  $y$ -momentum are defined as the covariance of velocity fluctuations  $\langle u' w' \rangle$  and  $\langle v' w' \rangle$ , respectively. Based on a Reynolds decomposition  $u = \bar{u} + u'$ , the mean velocities  $\bar{u}$  and fluctuating parts  $u'$  are obtained from the highpass filtered velocity components with an appropriate cut-off frequency  $\sigma_c$ , and similar for  $v$  and  $w$ . The average  $\langle \rangle$  represents a lowpass filter of the product of the fluctuating parts, with the same cut-off frequency in both filters.

An ADCP measures Doppler velocities  $b_i$ ,  $i=1$  to 4 along four slanted beams from which three velocity components  $\hat{u}, \hat{v}$  and  $\hat{w}$  in a Cartesian co-ordinate system are estimated. Only if the flow field is homogeneous across the beam spread, these estimates represent the true velocity vector  $(u, v, w)$ . This operation method has profound implications on determining momentum fluxes. The slant angle  $\delta$  of the four beams is  $30^\circ$  for our 1200 kHz ADCP and  $20^\circ$  for the 600 kHz ADCP, yielding a beam spread  $>10$  m at the uppermost velocity bin at 15 m range. However, for shear stress estimates using a four-beam ADCP it is not necessary that each beam measures the same instantaneous velocity field, which would restrict the resolved eddies to scales larger than twice the beam spread.

In fact, assuming *statistical* homogeneity of the velocity field, vertical fluxes of horizontal momentum may be estimated as  $\overline{u' w'} = \langle u' (w' - e') \rangle$ ,  $\overline{v' w'} = \langle v' (w' + e') \rangle$  in the  $x$ - and  $y$ -direction, respectively (Van Haren et al., 1994). These esti-

mates are the average over the beam spread of flux estimates within the width of each of the beams. The so-called error velocity  $e$ , which is a measure of the current inhomogeneity and which is calculated from the velocity differences obtained by different beam pairs, is essential in estimating momentum fluxes from ADCP data. Raw error velocities are a standard output of the utilised RDI broadband ADCP's and the recorded values have to be scaled by  $4\cos\delta$  to match the definition of the true velocity components. The vertical Reynolds stress component can be estimated as  $\overline{w'^2} = (\hat{w}' + \hat{e}')(\hat{w}' - \hat{e}')$  (Gemmrich and Van Haren, 2002).

The choice of the cut-off frequency  $\sigma_c$  has to fulfil physical as well as practical requirements. Studying mixing processes, the scales considered are ideally within the so-called inertial sub-range, where energy is cascaded down from energy containing eddies to dissipation scales. However, the given ADCP geometry, with velocity bins up to 1 m, does not allow resolving the latter (small) scales. Here, the focus is on mixing contribution from non-linear motions within the internal wave band, ubiquitous in the ocean.

For BBB96 we found a suitable cut-off frequency  $\sigma_c=15$  cpd at which the KE-spectrum changed slope (Gemmrich and Van Haren, 2002). However, changing it to  $\sigma_c=22$  cpd resulted in less than 5% change in flux values. For a consistent comparison, the same cut-off frequency  $\sigma_c=15$  cpd is used here for both data sets. In addition, contributions by the semidiurnal tide are examined with a cut-off  $\sigma_c=1.9$  cpd, which includes nearly the entire internal wave band in the fluctuating signals (at mid-latitudes).

In practice, mean and fluctuating parts were separated with a third order high-pass elliptic filter, applied in forward and reverse direction in order to eliminate phase shifts. This filter assured that for the cut-off frequency of 1.9 cpd the semidiurnal tidal signal is fully included in the fluctuating part of the signal. No high-frequency pre-filtering was applied and the obtained fluxes cover the specified internal wave band, including large turbulence scales up to the Nyquist frequency, well beyond the buoyancy frequency  $N$ .

To determine the statistical significance of our flux estimates we used a method which has been suggested by Ruddick (pers. comm., 1990), and described earlier (Yamazaki and Osborn, 1993; Fleury and Lueck,

1994; Van Haren et al., 1994; Gemmrich and Van Haren, 2002). According to this method, a flux estimate is considered to be statistically significantly different from zero if it falls outside the confidence interval of the distribution of the lagged covariance of the two fluctuating quantities. We find momentum flux magnitudes larger than  $\sim 5 \times 10^{-6} \text{ m}^2 \text{ s}^{-2}$  (PROV99) and  $10^{-5} \text{ m}^2 \text{ s}^{-2}$  (BBB96) are significantly different from zero at the 95% level.

For PROV99 vertical fluxes of momentum ( $\sigma_c=15$  cpd) in along-shore  $\overline{v' w'}$  and on-shore  $\overline{u' w'}$  and vertical direction  $\overline{w' w'}$  are of similar magnitude, up to  $10^{-4} \text{ m}^2 \text{ s}^{-2}$  (Fig. 7). The 7-d mean fluxes are  $O(-10^{-5} \text{ m}^2 \text{ s}^{-2})$  in along-shore, on-shore and  $O(2 \times 10^{-5} \text{ m}^2 \text{ s}^{-2})$  in vertical direction, respectively. On-shore fluxes are strongest at  $\sim 5\text{--}8$  m above the bottom. The resolved near-bottom layer reveals a semidiurnal tidal pattern consistent with a constant stress layer flow. Weak fluxes alternate with strong downward fluxes, occurring at the current maxima. The height of this layer, which is not apparent in the on-shore component, is  $\sim 5\text{--}7$  m.

A signature of the wind event can be seen in all three momentum-flux components. Near the surface the horizontal momentum flux components increase slightly, but there is a noticeable modification at mid-depth. The vertical component reaches values of  $O(10^{-4} \text{ m}^2 \text{ s}^{-2})$  when the along-shore component reaches the strongest downward fluxes of  $O(-10^{-4} \text{ m}^2 \text{ s}^{-2})$  and it may represent a conversion of along-shore momentum into vertical momentum. These enhanced fluxes did not occur until yearday 96, almost 24 h after the increase in wind speed. However, the occurrence of enhanced fluxes corresponds well with the period of significant wave heights  $>1$  m. It is likely that the change in momentum fluxes is of wave-induced rather than direct wind-induced nature.

Momentum fluxes for BBB96 are discussed in detail in Gemmrich and Van Haren (2002). In the mean, fluxes of along-slope momentum are positive. In cross-slope direction these fluxes are negative. In along-slope as well as cross-slope direction, fluxes of horizontal momentum are highly variable with time. For short periods, fluxes exceed the mean values by more than one order of magnitude. These events are most frequent during spring tide, occurring at irregular intervals up to five times per day, with no obvious relation to the mean current. Mag-

nitude of peak values are  $O(5 \times 10^{-4} \text{ m}^2 \text{ s}^{-2})$  and are similar in both directions. These values are about an order of magnitude larger than during PROV99. No indication of a constant stress layer is found near the bottom.

### 3.2. Kinetic energy production

The production  $P$  of kinetic energy in the high frequency range of the internal wave band (IWB-KE) is calculated according to (1) from the fields of momentum fluxes multiplied by the corresponding component of the mean velocity shear (shear stress contributions) and buoyancy contributions. Since no high frequency cut-off is employed, this estimate includes KE production from large turbulence scales, as long as they were resolved by the bin sizes within the beams of the ADCP's.

For PROV99 strongest shear stress contributions are in the along-shore direction (Fig. 8). Note that weak momentum fluxes with magnitudes  $< 5 \times 10^{-6} \text{ m}^2 \text{ s}^{-2}$  are statistically not significantly different from zero. Therefore, estimates of KE production associated with weak momentum fluxes are unreliable, resulting in apparently negative KE production. Lu and Lueck (1999) argue that non-stationary currents during flow reversal are causing negative KE- production estimates. We find periods of apparently negative KE production longer than can be explained by flow reversal. Particularly in the on-shore direction no significant correlation between negative KE production and flow reversal can be found. However, negative production rates not associated with weak momentum fluxes could imply transfer of energy from scales within the high frequency internal wave band ( $\sigma > 15$  cpd) to larger scales ( $\sigma \ll 15$  cpd).

Production rates in the along-shore direction are  $O(10^{-6} \text{ m}^2 \text{ s}^{-3})$  in the beginning of the experiment but reach  $O(10^{-5} \text{ m}^2 \text{ s}^{-3})$  during the wind event at yearday 96–97. Throughout the deployment a weak semidiurnal pattern of  $P$  is detectable. In the lower part of the water column the on-shore component of the shear stress contribution is mainly negative. The total shear stress contribution resembles the along-shore component with a somewhat more pronounced semidiurnal cycle. Despite significant fluxes of vertical momentum, the shear production in the vertical

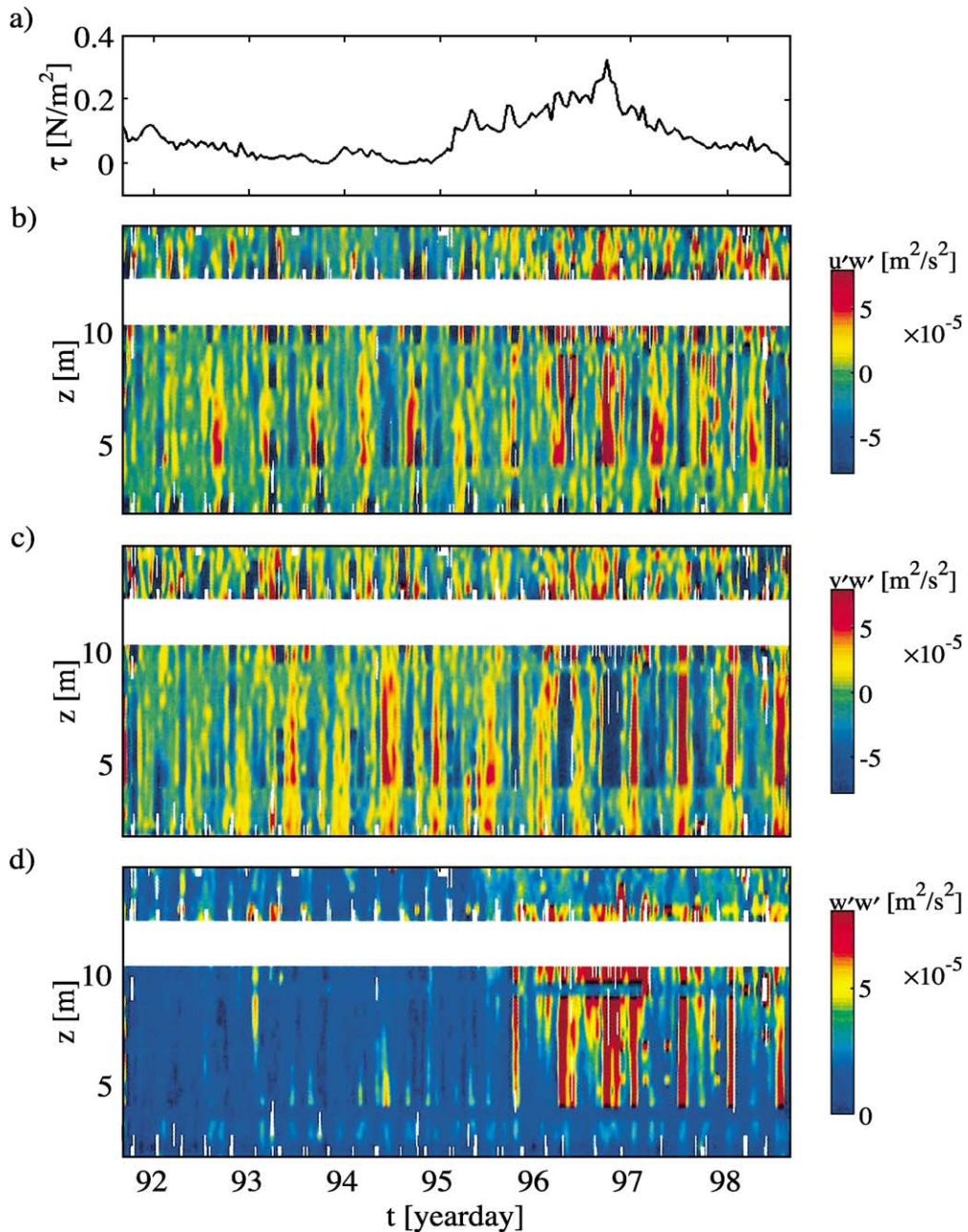


Fig. 7. Momentum fluxes at PROVESS99 for frequency band  $\sigma > 15$  cpd. (a) wind stress  $\tau$ . (b) on-shore component  $\overline{u'w'}$ , (c) along-shore component  $\overline{v'w'}$ , (d) vertical component  $\overline{w'w'}$ . (Intermittent interference with the thermistor string causes unreal low flux values around 3.5 m and 9.5 m. Fluxes at 10.65–12.65 m are unreliable due to strong interference with floatation and are not shown).

$\overline{w'w' \frac{\partial \bar{w}}{\partial z}}$  (not shown) is 2–3 orders of magnitude smaller than the horizontal components, which were comparable in magnitude (Fig. 8a,b). IWB-KE pro-

duction in the near-surface layer clearly mimics the wind stress, with larger values on yearday 92 and from yearday 95 onwards.

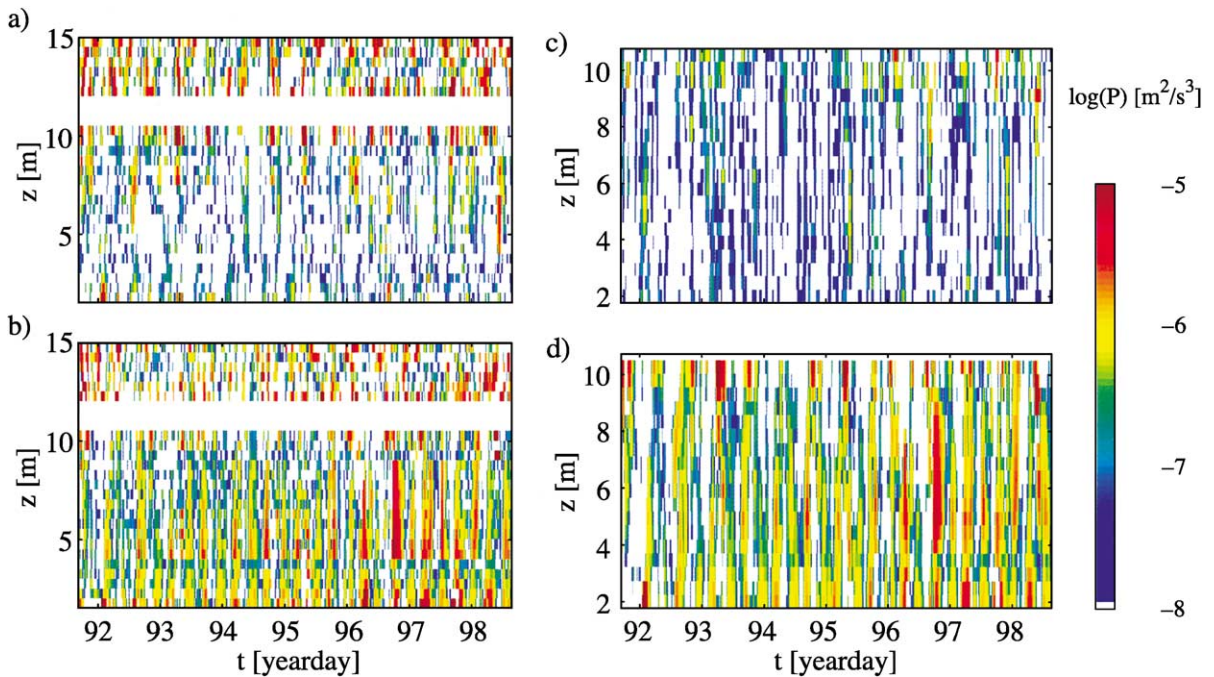


Fig. 8. Kinetic energy production at PROVESS99 for frequency band  $\sigma > 15$  cpd. (a) on-shore shear stress component  $\overline{u' w' \frac{\partial u}{\partial z}}$ , (b) along-shore shear stress component  $\overline{v' w' \frac{\partial v}{\partial z}}$ , (c) buoyancy production (blank areas represent KE-sinks), (d) total IWB-KE production. Blank areas in (a), (b), (d) represent unresolved or insignificant values. (Note different vertical scales).

Buoyancy KE production  $BP$  is only available within the coverage of the thermistor string (Fig. 8c). The buoyant production term alternates between positive values (KE source) and negative values (KE sink). Both, sources and sinks are comparable in magnitude. Despite the relatively strong stratification at the PROVESS99 site,  $BP$  sources and sinks are approximately two orders of magnitude smaller than the shear stress contribution and play a negligible role in the total IWB-KE production  $P$  (Fig. 8d).

$P$  is strongest in the near-bottom layer as well as the near-surface layer. Production maxima at 10 m height are delayed by a phase shift of 4–5 h compared to the bottom. A similar phase shift can be seen in the dissipation obtained from microstructure profiles (Fisher et al., 2002). A noticeable exemption occurs on yearday 96.6 when the maximum of  $P$  is found at 4–8 m above the bottom and the phase shift becomes negligible. This mid-depth maximum is also the largest overall value during the deployment period. It is related to the increased wind speed. No significant change of the along-shore current field is asso-

ciated with this wind event, whereas the on-shore current weakens significantly and the  $180^\circ$  phase shift between surface and bottom flow disappears. It is likely that the energy input from the wind is transferred via surface waves to turbulence. Associated mixing reduces stratification which in turn slows down the cross-shore current component (Visser et al., 1994).

The role of low frequency internal waves in kinetic energy production is evaluated using a cut-off frequency  $\sigma_c = 1.9$  cpd (Fig. 9). On average, kinetic energy production in this broader frequency range is approximately five times larger than KE production in the high frequency range (compare Figs. 8d and 9). The magnitude of KE production at  $\sigma > 1.9$  cpd is in good agreement with turbulence dissipation rates estimated from microstructure profiler measurements in the vicinity (Fisher et al., 2002). Largest KE production at  $\sigma > 1.9$  cpd occurs just above mid-depth with duration of one to two tidal cycles on days 95–96. Large KE production is well correlated with enhanced stratification (Fig. 4).

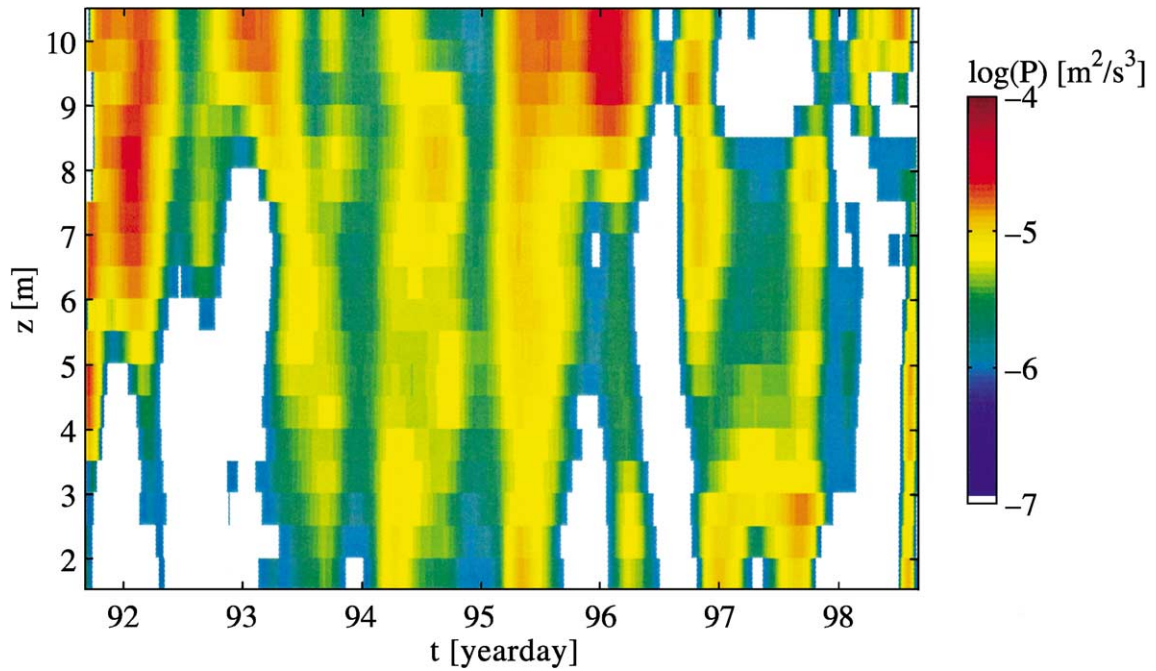


Fig. 9. Total IWB-kinetic energy production at PROVESS99 at frequency band  $\sigma > 1.9$  cpd. Blank areas represent unresolved or insignificant values.

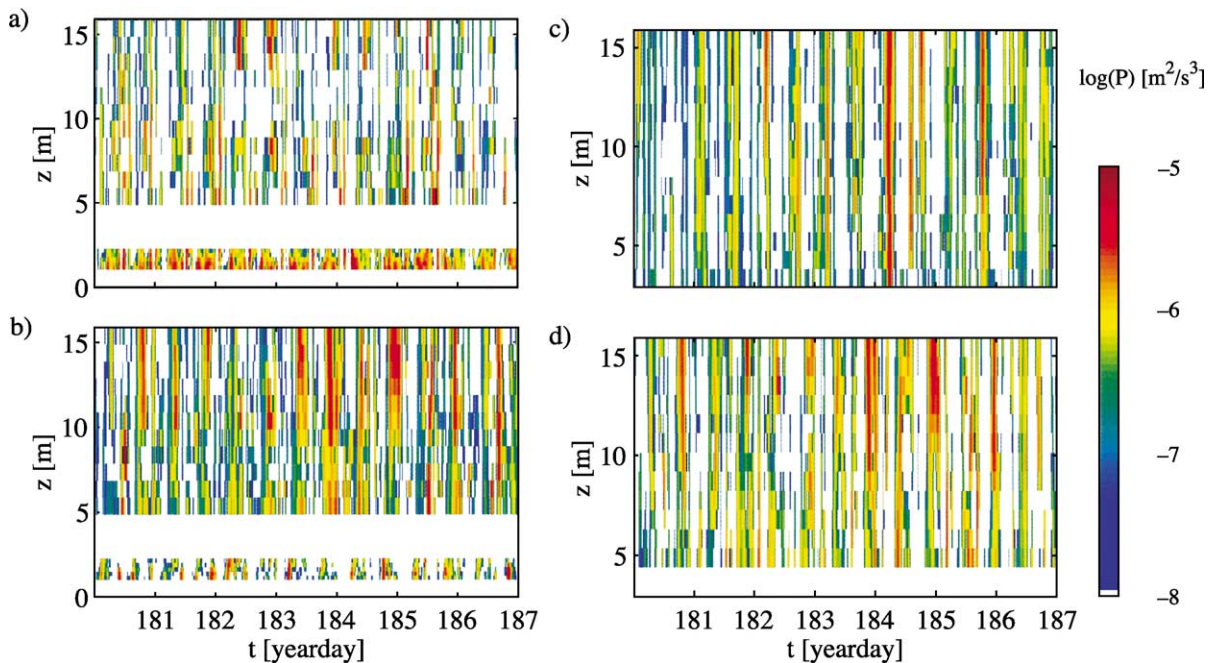


Fig. 10. Kinetic energy production at BBB96 for frequency band  $\sigma > 15$  cpd. (a) along-slope shear stress component  $\overline{u'w'} \frac{\partial v}{\partial z}$ , (b) cross-slope shear stress component  $\overline{v'w'} \frac{\partial v}{\partial z}$ , (c) buoyancy production (blank areas represent KE-sinks), (d) total IWB-KE production. Blank areas in (a), (b), (d) represent unresolved or insignificant values. (Note different vertical scales).

At BBB96, a two-layer system is apparent in IWB-KE production ( $\sigma > 15$  cpd). In the near-bottom layer (below 3 m) production takes place mainly in the along-slope direction, whereas above 5 m the cross-slope direction contributes mostly to  $P$  (Fig. 10). Maximum shear stress contributions of  $O(10^{-5} \text{ m}^2 \text{ s}^{-3})$  are found in the near-bottom layer. These values are comparable with those estimated during strong wind events at PROVESS99. The weakest shear stress IWB-KE production occurs at  $\sim 5$  m and above that level values increase with distance to the bottom. A strong semidiurnal pattern is seen in the total shear stress contribution as well as in  $BP$ . Magnitudes of  $BP$  are up to 10 times greater during periods of positive  $BP$  than in periods when  $BP$  represents a sink of kinetic energy. In contrast to PROVESS99, the positive buoyancy contribution is comparable to the shear stress contributions. The largest overall production occurs slightly after the current maximum and reaches  $> 10^{-5} \text{ m}^2 \text{ s}^{-3}$ .

Overall IWB-KE production (for 15 cpd cut-off frequency) is somewhat larger in the sloping bottom layer at BBB96 than within the flat energetic site at PROVESS99. The larger KE production during BBB96 is not only caused by larger buoyant production  $BP$ . At PROVESS99 even the shear-stress KE production is less during strong tides and wind than at the site above the sloping bottom.

#### 4. Summary and discussion

We have presented a study of kinetic energy production in two contrasting environments. Rms currents at a shallow flat site within the Rhine region of fresh-water influence are  $1.3 \text{ m s}^{-1}$ . The strongest kinetic energy production for  $\sigma > 15$  cpd occurs in the near-bottom layer and is mainly induced by bottom-friction. However, following the bulk method  $\overline{u'w'} = C_D u^2$ , corresponding momentum fluxes imply a low value of the drag coefficient  $C_D < 1 \times 10^{-3}$ . Shear stresses in the near-surface layer generate a second layer of significant KE production. Despite a strong mean stratification at the site, the buoyant KE production is negligible when compared to shear stress KE production. During calm wind periods, KE production is up to one order of magnitude smaller at mid-depth than in the bottom boundary and surface boundary regions.

A distinct mid-depth maximum of KE production is caused by wind- and wave-mixing. A consequence of this KE production is increased mixing and reduced stratification, which in turn slows down the stratification-driven cross-shore current shear. The low-frequency ( $< 1.9$  cpd) along-shore current seems not to be modified by the atmospheric momentum input. This suggests that the energy input takes place directly into turbulence scales.

Kinetic energy production at frequencies  $\sigma > 1.9$  cpd, including the semidiurnal tide, is largest where strong stratification is present.

At the site above the continental slope, where tidal currents are much weaker, the buoyant KE production is comparable with the shear production. Bottom friction results in strong shear production in a shallow near-bottom layer. The height of this frictional dominated layer is less than 5 m, but no data are available to further constrain the height. Above 5 m, shear production and total KE production increase with distance from the bottom. At this site internal waves could reflect at the sloping bottom, resulting in strong internal wave shear several metres above the bottom. Hence, outside the shallow near-bottom layer, KE production is based on internal wave shear rather than bottom friction. The overall KE production in the sloping boundary layer is somewhat larger than above the flat bottom, despite weaker currents and weaker stratification. This supports the idea of relatively strong boundary mixing at continental slopes. Furthermore, assuming a balance of KE production and dissipation implies that regions of rough bottom topography may contribute significantly to tidal dissipation.

#### Acknowledgements

The North Sea data were acquired and analysed within the PROVESS project, funded by the European Union under contract MAS3-CT097-0159. The BBB96-data were acquired during the Bay of Biscay Boundary project, funded by the Netherlands Organization for Scientific Research (NWO). J.G. was partially supported by a European Union TMR research fellowship under contract MAS3-CT97-5047. We thank the crews of *R/V Pelagia* for their help in deployment and recovery of our instrumenta-

tion during both projects. The scientific analysis benefited from discussion with Leo Maas. This is NIOZ contribution no. 3580.

## References

- DeSilva, I.P.D., Imberger, J., Ivey, G.N., 1998. Breaking of super-critically incident internal waves at a sloping bed. *Physical Processes in Lakes and Oceans*. *Coast. Estuar. Stud.* 54, 475–484.
- Eriksen, C.C., 1985. Implications of ocean bottom reflection for internal wave spectra and mixing. *J. Phys. Ocean.* 15, 1145–1156.
- Fisher, N., Simpson, J.H., Howarth, M.J., 2002. The cycle of dissipation in the region of freshwater influence. *J. Sea Res.*, in press.
- Fleury, M., Lueck, R.G., 1994. Direct heat flux estimates using a towed vehicle. *J. Phys. Oceanogr.* 24, 801–818.
- Gemmrich, J.R., Van Haren, H., 2002. Internal wave band eddy fluxes above a continental slope. *J. Mar. Res.* 60, 227–253.
- Ivey, G.N., Nokes, R.I., 1989. Vertical mixing due to the breaking of critical internal waves on sloping boundaries. *J. Fluid Mech.* 204, 479–500.
- Lohrmann, A., Hackett, B., Røed, L.P., 1990. High resolution measurements of turbulence, velocity and stress using a pulse to pulse coherent sonar. *J. Atmos. Ocean. Tech.* 7, 19–37.
- Lu, Y., Lueck, R.G., 1999. Using a broad band ADCP in a tidal channel. Part II: Turbulence. *J. Atmos. Ocean. Tech.* 16, 1568–1579.
- McCandliss, R.R., Jones, S.E., Hearn, M., Latter, R.J., Jago, C.F., 2002. Dynamics of suspended particles in coastal waters (southern North Sea) during a spring bloom. *J. Sea Res.* 47, 285–302, this issue.
- Simpson, J.H., Souza, A.J., 1995. Semidiurnal switching of stratification in the Rhine ROFI. *J. Geoph. Res.* 100, 7037–7044.
- Van Haren, H., Garrett, C., Oakey, N., 1994. Measurements of internal wave band eddy fluxes above a sloping bottom. *J. Mar. Res.* 52, 909–946.
- Van Haren, H., Groenewegen, R., Laan, M., Koster, B., 2001. A fast and accurate thermistor string. *J. Atmos. Ocean. Tech.* 18, 256–265.
- Visser, A.W., Souza, A.J., Hessner, K., Simpson, J.H., 1994. The effect of stratification on tidal current profiles in a region of freshwater influence. *Oceanol. Acta* 17, 369–381.
- Yamazaki, H., Osborn, T., 1993. Direct estimation of heat flux in a seasonal thermocline. *J. Phys. Oceanogr.* 23, 503–516.